JOURNAL OF MATERIALS SCIENCE 35 (2000) 4251–4260

Microstructure and the influence of spontaneous strain in $LaCoO_3$, $La_{0.8}Sr_{0.2}CoO_3$ and $La_{0.8}Ca_{0.2}CoO_3$

J. C. WALMSLEY, A. BARDAL
SINTEF Materials Technology, N-7465 Trondheim, Norway
E-mail: asgeir.bardal@matek.sintef.no

K. KLEVELAND, M.-A. EINARSRUD, T. GRANDE
Department of Chemistry, Norwegian University of Science and Technology, N-7491 Trondheim, Norway

Transmission Electron Microscopy has been conducted on rhombohedral perovskite oxides with composition $LaCoO_3$, $La_{0.8}Sr_{0.2}CoO_3$, and $La_{0.8}Ca_{0.2}CoO_3$. Thin foils prepared within the first weeks of sintering showed macroscopic strain and a very high defect density, which included fault-related superlattice structures. Samples prepared several months after sintering, showed no significant macroscopic strain and the main defect was found to be domains due to reflection twinning in the pseudo-cube plane. The behaviour is likely to be related to accomodation of spontaneous strain arising upon cooling of the material from the sintering temperature. The presence of twin domains illustrates the lowering of lattice symmetry as compared to the ideal cubic perovskite structure, and is relevant for explaining recent observations of ferroelastic behaviour of these materials. © *2000 Kluwer Academic Publishers*

1. Introduction

Lanthanum cobaltites are ABO_3 perovskites in which a proportion of the A-site La cations may commonly be substituted by divalent atoms like Sr or Ca. Lanthanum cobaltites are of considerable industrial interest. They have high electrical and ionic (O^{2-}) conductivities and are considered for use as cathode materials in solid oxide fuel cells, oxygen permeable membranes and are active catalysts for oxidation of CO. Physical properties of these materials have been studied extensively [1–6]. Less attention has been paid to characterisation of the microstructure and studies have focussed on epitaxial films with a relatively high degree of substitution [7, 8].

At room temperature the lanthanum cobaltites considered here belong to the rhombohedral space group $R\bar{3}c$. A tilting of the cobalt-oxygen octahedra yields a slight distortion of the ideal cubic perovskite structure along one body diagonal. Some structural data on these compounds can be found in the literature [1, 4]. An effect of Sr or Ca substitution is to reduce the rhombohedral distortion. At room temperature (RT) the rhombohedral angle for $La_{1-x}Sr_xCoO_3$ falls as x increases from zero, and the structure becomes cubic for $x = 0.5$. Mineshige *et al*. [4] report lattice parameters of $a = 5.38$ Å and $\alpha = 60.8^\circ$ at RT for $LaCoO_3$, changing to 5.40 Å and $\alpha = 60.55^\circ$ for a Sr substitution level of 20%. Detailed structural data on the Ca-substituted system is not available in the literature. $LaCoO_3$ is rhombohedral up to at least 1000 °C [9, 10], whereas studies by Orlovskaya *et al*. [11] indicate that the transition to cubic symmetry is above 1100 °C. The transition temperatures for $La_{0.8}Ca_{0.2}CoO_3$ and $La_{0.8}Sr_{0.2}CoO_3$ are about 950 °C and 900 °C, respectively [10].

The initial objective of our study was to characterise the microstructure of sintered non-substituted, Sr-substituted and Ca-substituted material in the Transmission Electron Microscope (TEM), with a focus on possible segregation and cation ordering effects. However, we made rather unexpected observations of highly defective microstructures, which are presented here and discussed in the context of the basic crystallography of the material and spontaneous strain arising from thermal stress introduced during cooling from the sintering temperature. The observations are relevant to recent observations of ferroelastic behaviour of similar materials [11].

2. Materials and methods

The powders were prepared by a wet chemical route using ethylenediamine tetra acetate acid (EDTA) as a complexing agent, and calcined at 900–1000°C for 8–72 h as described by Kleveland *et al*. [12]. The powders were ball milled before and after calcination. Material was sintered as cylindrical pellets, ~8 mm in diameter and 5 mm deep, at 1200°C for 24 h. After sintering the cooling rate was ~1000°C/h. One of the pellets was later annealed at 900°C for 120 h with a subsequent cooling rate of 10°C/h. Three compositions were prepared, $LaCoO_3$, $La_{0.8}Sr_{0.2}CoO_3$, and $La_{0.8}Ca_{0.2}CoO_3$.

After sintering, the densities of the materials were 98.6% ($LaCoO_3$) and 98.8% (substituted materials).

Because of the observations that have been made, the TEM sample preparation procedure and sequence is described precisely. The pellets were attached to a cylindrical steel mount and slices ∼0.5 mm thick were cut using a diamond-impregnated cutting wheel. The first slice cut was put to one side and a second slice was cut which was expected to be more representative of the bulk material. One of the undoped pellets was damaged during initial cutting and some cracks were introduced. 3 mm diameter discs were cut from each slice using an ultrasonic disc cutter. Each slice was approximately 300 μm thick. Up to four complete discs were obtained from each slice, depending of the presence of pre-existing cracks. The discs were mechanically ground to 100–200 μm thickness using wet silicon carbide paper of #1200 grade. Discs were "dimpled" on one side using a Gatan model 656 Dimple Grinder and 4–8 μm diamond paste to a central thickness of ∼35 μm. Mechanically thinned discs were ion-beam-thinned using a Gatan duo-mill operating at 3.5–4 kV and a thinning angle of ∼11.5°. X-ray diffraction (XRD) was performed with a Siemens D5005 diffractometer using Cu K_α radiation and a secondary monochromator, in the 2θ range of 20–65° with a step time of 9.0 seconds. TEM was performed with a Philips CM30 microscope. Examination was conducted at a beam voltage of 300 kV.

3. Results

Powder XRD was done shortly after sintering and after crushing the sintered pellets. The diffractograms were consistent with single-phase $LaCoO_3$ and reported powder diffraction data, i.e. space group $R\bar{3}c$ and lattice parameters as shown in Table I. Levels of secondary phase were sufficiently low that no additional diffraction peaks were detected. SEM observations of etched surfaces also suggested low levels of secondary phases, Fig. 1, although secondary phases could have been etched away. Average grain sizes were measured as 4.8 μm for the non-substituted material, 4.0 μm for the Sr-substituted material and 2.9 μm for the Ca-substituted material.

TEM samples prepared <1 month after sintering revealed significant residual stresses in the materials.

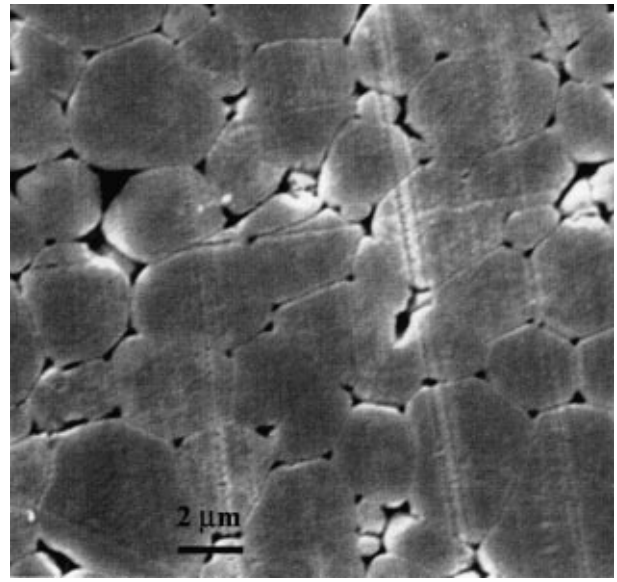

Figure 1 SEM image of etched $LaCoO_3$ surface showing typical grain sizes.

These samples exhibited unexpected, highly defective micro-structures and diffraction patterns revealed superlattice reflections. TEM samples prepared 5 months later from the same materials showed no evidence of residual stress, and exhibited microstructures one might well have anticipated before starting the investigations. For clarity, we will first describe the "well-behaved" microstructures of the unstrained material, prepared in the second preparation campaign. We then describe the "ill-behaved" microstructures found in samples prepared shortly after sintering.

3.1. Samples with "well-behaved" microstructures-prepared 5 months after sintering

Thin foils were prepared from the original pellets approximately 5 months after the pellets were sintered. These foils were from 3 mm diameter discs that had been punched, but not ground, during the first campaign of sample preparation or from slices cut from immediately next to them. During thinning, the samples showed no evidence of distortion or relaxation of residual strain. The defect density of the material was comparatively

TABLE I Summary of preparation and TEM observations

Material and measured lattice parameters (RT)	Prepared <1 month of sintering	Prepared >5 months after sintering
$LaCoO_3$	Residual stress and cracking of sample.	No residuals stress. No superlattice.
$a = 5.379$ Å, $\alpha = 60.79°$		
$La_{0.8}Ca_{0.2}CoO_3$	Deformation superlattice and high defect density.	Low defect density.
$a = 5.377$ Å, $\alpha = 60.68°$		
$La_{0.8}Sr_{0.2}CoO_3$	Superlattice and defect structure stable w.r.t time.	Reflection twinning on $\{100\}_c$.
$a = 5.403$ Å, $\alpha = 60.55°$		
$LaCoO_3$ Annealed 900°C/120 h	Similar to above	Similar to above
$LaCoO_3$ Cracks introduced <1 month after sintering	Not observed	No residual stress. Limited deformation superstructure in some grains.

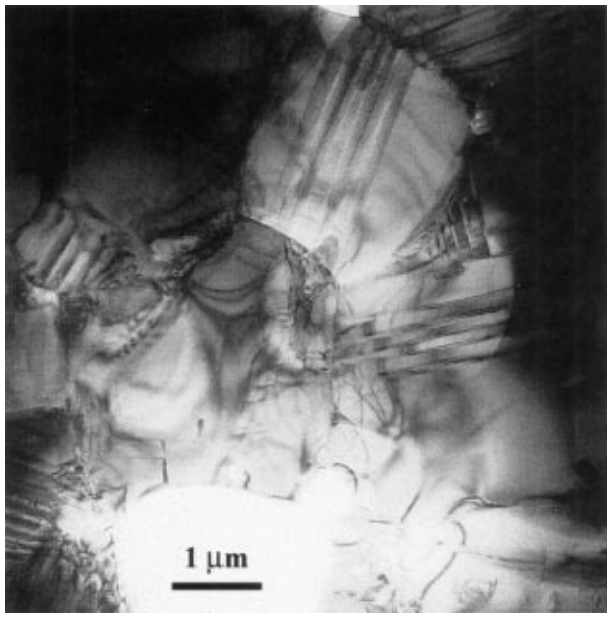

Figure 2 Bright-field TEM image showing twin domains in most grains. The foil was prepared 5 months after sintering and exhibited "well-behaved" microstructures.

low. With one exception (described below), there was no evidence of a superlattice in the diffraction patterns from TEM foils prepared from any of the three material compositions. Fig. 2 shows a low magnification image of the typical microstructure, taken from one of the non-substituted material samples.

The $R\bar{3}c$ $LaCoO_3$ structure is commonly described on the basis of rhombohedral axes, defining a primitive rhombohedral cell with a rhombohedral angle α close to 60°, or equivalently on a hexagonal basis. In addition, while interpreting TEM observations, it is convenient to describe the structure as primitive pseudo-cubic. The angle between the pseudo-cube ⟨101⟩ directions (exactly 60° in the cubic case) then corresponds to the α angle in the rhombohedral description. In this way defects and diffraction patterns can easily be visualised in relation to both the phase transformation and the ideal perovskite structure. Here we adapt to two indexing conventions, the pseudo-cubic (index c) and the hexagonal description of the rhombohedral cell using the Miller 3-index notation.

Twin domains were commonly observed in all three materials and they are the most obvious features evident in Fig. 2. The twin habit planes are parallel to the pseudo-cube $\{010\}_c$ planes. The twin domain boundaries are also nearly parallel to $\{100\}_c$, but exhibit some curvature. This is illustrated clearly in Fig. 3a, where a grain is viewed along a direction near $[001]_c$ and two intersecting twin orientations are viewed edge-on. The orientation is shown in the corresponding diffraction pattern, Fig. 3b. Some twins have a needle shaped morphology, with variable needle sharpness. The density of twin boundaries is often higher around grain edges where the intersection pattern of twin orientations can be quite complicated. Most of the twins visible in Fig. 3 lie on (100) and (010), twinning may also occur on (001), close to the plane of the foil.

The crystallography of the twins is confirmed by closer examination of diffraction patterns obtained with the selected area aperture positioned to include material on either side of one or more boundaries, Fig. 3c. While the $(0\bar{1}2)/(010)_c$ systematic row is common to both sides of the boundary, it can be seen that positions of the $(\bar{1}1\bar{2})/(100)_c$ reflections are separated by a small displacement along $[01\bar{2}]$. This is consistent with performing a reflection operation in the (012) twin plane. The relationship between the alignment of planes on either side of the twin plane and the diffraction pattern is illustrated schematically in Fig. 3d. The splitting of the $(\bar{1}1\bar{2})$ reflections arising from the crystals below and above the twin boundary reflects the lowering of symmetry during the cubic to rhombohedral phase transition. The measured angle between the $(\bar{1}1\bar{2})$ and $(\bar{1}1\bar{2})_t$ g-vectors (1.4°), and the measured difference between the length of the $(10\bar{4})$ and $(\bar{1}20)$ g-vectors $(2(g1-g2)/(g1+g2) = 1.2\%)$ are both consistent with the XRD observations ($\alpha = 60.79°$, $d_{104} = 2.688$ Å, $d_{120} = 2.719$ Å).

Other planar faults were observed in a small proportion of the grains examined in all three of the materials. These either had distinct $\{100\}_c$ habit planes or irregular habit planes. Both types of morphology are illustrated in Fig. 4, having the morphological characteristics of stacking-faults and anti-phase boundaries respectively. Most of the stacking faults formed closed circuits and they often displayed a stepped morphology. Fig. 4a shows a grain that was found to contain several closed stacking fault circuits, viewed close to a $[001]_c$ zone axis direction. It can be seen that the faults lie on $(100)_c$ and $(010)_c$, that the corners at changes of orientation are sharp and that a fine scale step structure is present at some positions. At least one section of stacking fault is not closed and must, therefore, be bounded by partial dislocations. While the stacking faults were not analysed thoroughly, contrast in images obtained under several diffraction conditions were consistent with earlier work where a displacement vector of $\frac{1}{2}[011]_c$ was found in $La_{0.5}Sr_{0.5}CoO_3$ (cubic) grown from the vapour phase [8]. The boundary crossing the grain in Fig. 4b is probably an anti-phase boundary, for which the most obvious displacement vector to be proposed is $\frac{1}{4}[111]_c$, but again no detailed analysis of the contrast was carried out. The density of perfect lattice dislocations in the materials was very low and only a few isolated examples of dislocations were observed.

3.2. Samples with "ill-behaved" microstructures-prepared few weeks after sintering

All the TEM foils prepared within about one month of sintering showed qualitatively similar thinning behaviour and microstructure. After perforation, the thin region for each material condition showed evidence of considerable residual strain. The thin central part of the sample deformed, was no longer parallel to the original plane of the sample and tended to crack. TEM analysis was made difficult by the fact that materials were found to be quite friable, small cracks were present and electron transparent grains were easily lost from the foil. The defect density of each material was found to

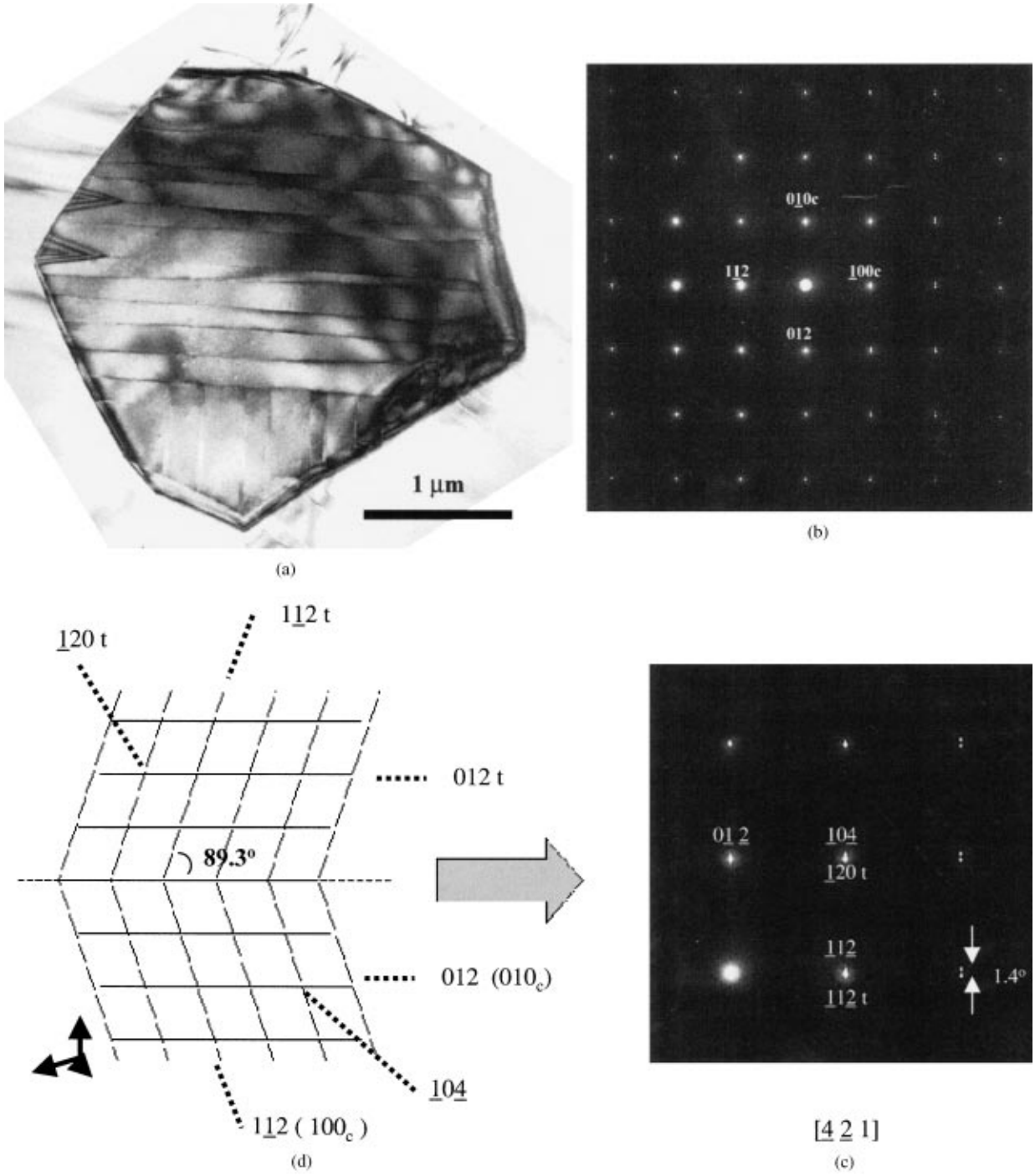

Figure 3 Details of reflection twin domains. (a) Bright-field image showing two sets of twin orientations. (b) Selected-Area Diffraction (SAD) pattern from centre of a, with horizontal twin boundaries. (c) Larger magnification of SAD pattern showing coincidence of (0$\underline{1}\underline{2}$) and splitting of ($\underline{1}\underline{1}2$) reflections (d) Schematic drawing of crystal orientation at reflection twin boundary, with indication of some major crystal planes (dotted). The angular distortion from 90° is exaggerated in the drawing.

be extremely high, Fig. 5. Diffraction patterns from all three compositions showed a superlattice structure. In the pattern of Fig. 5 the weaker superlattice reflections correspond to a tripling of the $(100)_c$ and $(010)_c$ pseudocube spacing of the rhombohedral structure. The pattern corresponds to the presence of two sets of domains, within the area defined by the selected area aperture, superlattice reflections being present along the two directions separately. The bright-field/dark-field image pair of Fig. 6 shows planar defects lying within twin domains in a single grain. The high planar-defect density produced streaking of reciprocal points and deliberate alignment of the foil to chosen diffraction conditions was difficult.

Fig. 7 shows diffraction patterns obtained from major zone axes in non-substituted $LaCoO_3$, in both the "well-behaved" and "ill-behaved" states. In the "well-behaved" state (Fig. 7a–c) all $\langle 100\rangle_c$ and all $\langle 110\rangle_c$ zone axes are symmetrically equivalent, while $\langle 111\rangle_c$ is the 3-fold axis and other $[111]_c$ zones axes are not equivalent to it. Diffraction patterns are indexed both in pseudo cubic and hexagonal notations. In Fig. 7b, we notice {$\underline{1}11$} reflections that violate extinction rules for $R\bar{3}c$. In the depicted zone axis the reflections can easily have

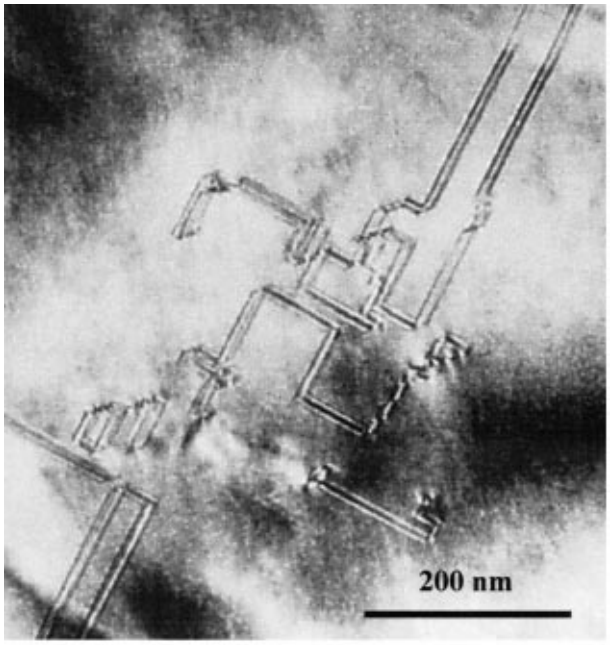

(a)

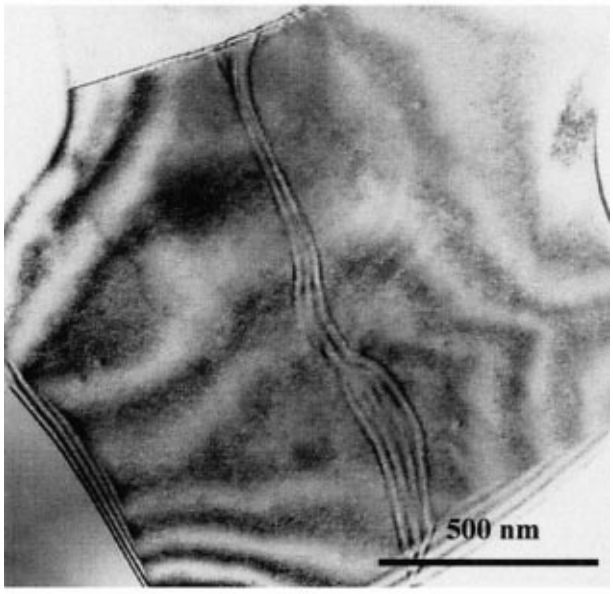

(b)

Figure 4 Characteristic, but less frequently encountered planar defects, with contrast characteristic of (a) stacking-fault and (b) anti-phase boundary.

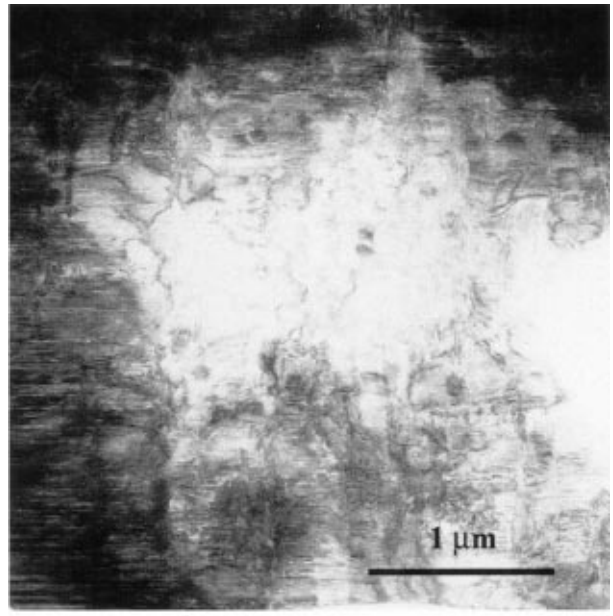

(a)

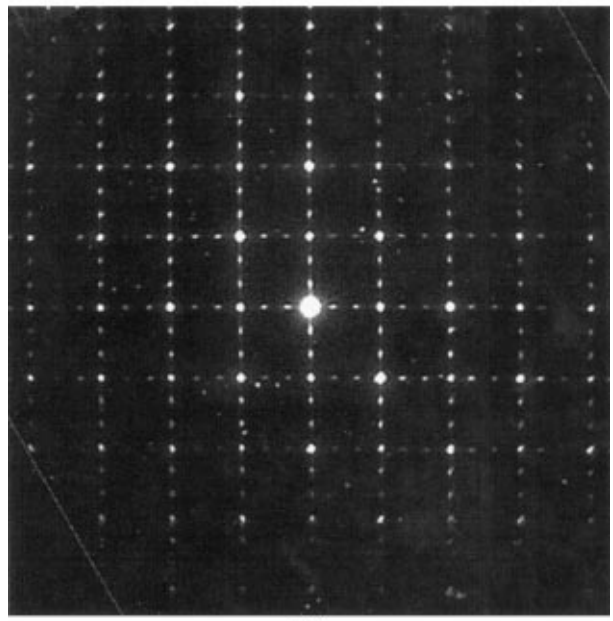

(b)

Figure 5 Typical microstructure of sample prepared shortly after sintering, and exhibiting "ill-behaved" microstructures. (a) Bright-field image showing high density of planar defects on two perpendicular sets of pseudo-cube planes, plus strain contrast. (b) SAD pattern showing superposition of two sets of domains viewed along $[001]_c$, with superstructure reflections along $(200)_c$ and $(020)_c$ respectively.

arisen by double diffraction, e.g. $\{\underline{1}23\} + \{0\underline{1}2\}$. We have, however, also observed the $\{\underline{1}11\}$ reflections under systematic-row conditions, under which they cannot be explained by double diffraction. The $\{\underline{1}23\}$ reflections are a consequence of the rhombohedral distortion, and cannot be indexed (using integers) on the primitive cubic basis. The reflections disappear as the rhombohedral distortion approaches zero. The diffraction patterns from the ill-behaved material (Fig. 7d and e) show a superstructure along $(0\underline{1}2)/(010)_c$. The dominant superstructure periodicity is a tripling of the $(010)_c$ spacing. Weak reflections having a different periodicity, i.e. a doubling of the (010) spacing, are also superimposed in the pattern. The superposition of a strong tripling superstructure and a weak doubling superstructure is a common situation encountered in the "ill-behaved materials. The angle between the (100) and (010) g-vectors in Fig. 7d is very close to 90° (equal within a measurement accuracy of ±0.1°), showing that the rhombohedral distortion is much reduced in the ill-behaved materials with superstructures (the corresponding angle in Fig. 7a is 89.3°). The presence in Fig. 7e of a systematic row of weak reflections along [012] (including $\{\underline{1}23\}$), suggests that there is still a slight rhombohedral distortion in the structure with the superlattice reflections.

In one of the Sr-doped material foils, it proved possible to remove the high general defect density and the superlattice reflections by focussing the electron beam onto a single grain for several minutes. In the image of Fig. 8a, the contrast of most of the grain shows

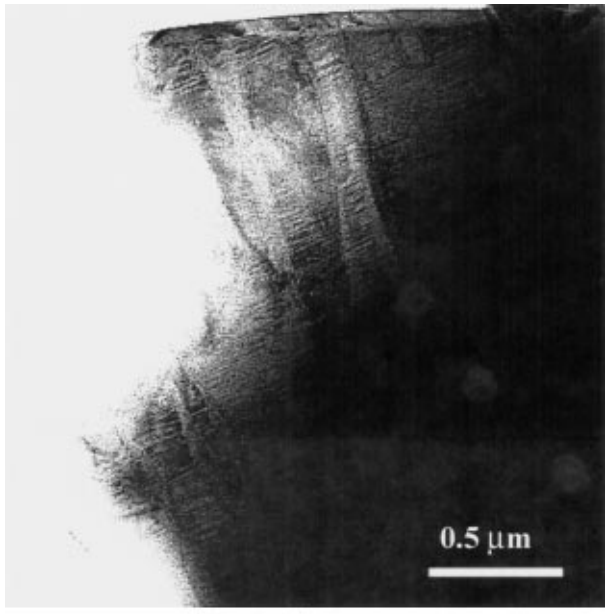

(a)

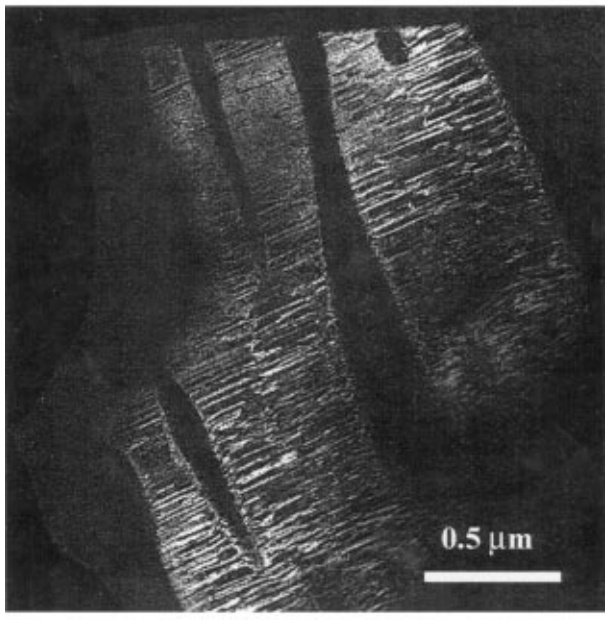

(b)

Figure 6 Defects in material with "ill-behaved" microstructures. (a) Bright-field image showing contrast in all domains. (b) Dark-field image showing contrast in one set of domains.

a uniform density of defects with approximately planar alignment and such a high density that individual faults are difficult to distinguish. Fig. 8b shows the [011] diffraction pattern recorded from the central part of the grain. Fig. 8c shows the same grain after exposure to an intense electron beam. The orientation of the foil is the same as that of Fig. 8a. Here, the complicated defect contrast of Fig. 8a has been replaced by mostly defect free clean single-domain contrast. The contrast that is present is mostly due to bend contours arising from bending of the foil due to low levels of strain. Several irregular planar faults with curved interfaces are visible. These were not analysed in detail but probably correspond to antiphase boundaries between regions where defect-free islands nucleated independently during annealing. The superlattice reflections have disappeared from the diffraction pattern, Fig. 8d, leaving a regular [001] diffraction pattern. The grain of Fig. 8 did not have continuous contact with the rest of the sample and would probably have been heated significantly by the electron beam. Other grains, in better thermal contact with the bulk of the sample, retained the defect structure under a focused beam and probably did not reach such a high temperature. This suggests that the change in the microstructure is due to localised heating of the sample rather than radiation damage.

There was one exception from the rule that "ill-behaved" microstructures were always found in samples from the first preparation campaign, and "well-behaved" microstructures in samples from the second campaign. Superlattice reflections were observed in diffraction patterns obtained from a single thin foil prepared from the very edge of the outer surface of an unannealed pellet of $LaCoO_3$, Fig. 9. The pellet was cracked by rough handling during the first sample preparation campaign, i.e. less than 1 month after sintering. The foil was prepared from a small, irregular, fragment ($\sim$2.5 mm $\times$ 2 mm) of material that remained after the sample slice was cut. The thin part of the foil was very close to the original crack and plastic deformation, due to stress relief, could easily have occurred in this part of the sample around the same time that thin foils showing a superlattice were prepared. An important feature evident in Fig. 9 is that, while the superlattice defect structure is present in most of the grain, some parts of the same grain are defect-free single crystal. Some twin domains can also be seen. The spherical feature at the centre of the field is either an inclusion of impurity or a region of misoriented cobaltite. The inclusion appears to have acted as a focus for strain in the material and the pattern of the deformation structure is centred upon it.

As a result of the observation of a high defect density in the material, one of the pellets of $LaCoO_3$ was annealed, Table I, and then prepared for TEM with a fairly large perforation. One foil of $LaCoO_3$ was further ion-thinned to enlarge the original perforation, to expose material where the sample showed less significant levels of macroscopic strain. In these foils, superlattice reflections were still present in diffraction patterns. The thin foils that originally showed the superlattice and deformation microstructure were re-examined at this stage (i.e. after five months) and were found to be essentially unchanged. The high defect density was still present and superlattice reflections were still present in diffraction patterns recorded from these grains.

We investigated the possibility that compositional inhomogeneity in the material may be responsible for the contrasting observations made between samples prepared shortly after sintering, and five months later. The samples prepared after five months were taken from different postions in the pellets, close to the surface and far from the surface, including equivalent positions to the samples that showed residual stresses after the first sample preparation campaign. A total of 7 TEM samples were prepared during the second preparation campaign, and a total of 4 samples during the first campaign. None of the foils prepared from the latter campaign showed residual stress during thinning and no deformation

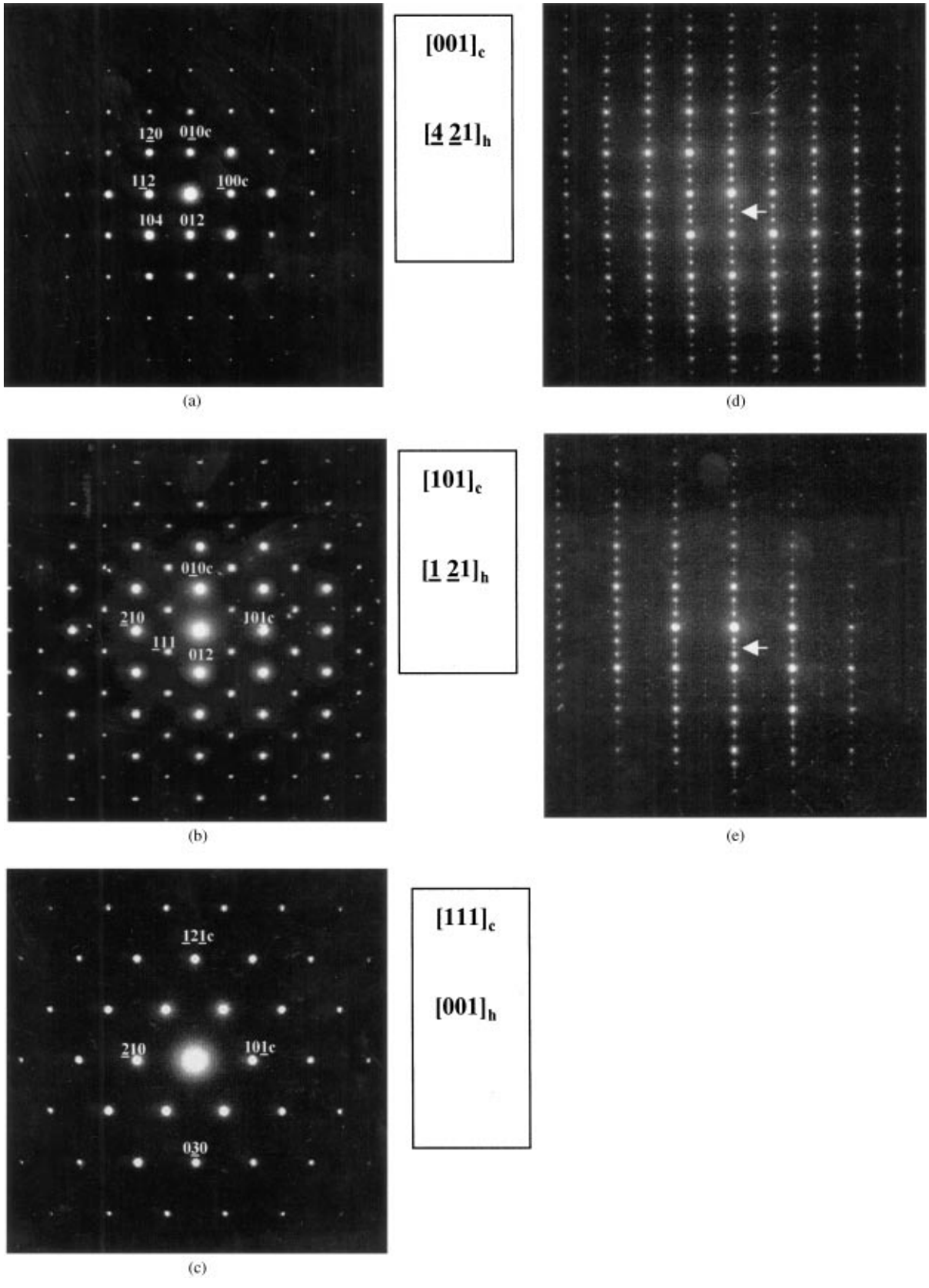

Figure 7 SAD patterns from material with "well-behaved" microstructures (a–c) and "ill-behaved" microstructures (d–e). (d and e) show superpositions of patterns corresponding to a tripling of the cell along $[010]_c$ or [012] (strong superstructure reflections) and a doubling along $[010]_c$ or [012] (weak, arrowed reflections).

superlattice reflections were present in diffraction patterns. The microstructure in all foils from the second preparation campaign was similar, i.e the defect content was low and the microstructure was dominated by $\{001\}_c$ twinning.

4. Discussion

It appears that the microstructure of these materials is dominated by the influence of spontaneous strain introduced possibly by the cubic to rhombohedral phase transition, and certainly by thermal stresses arising

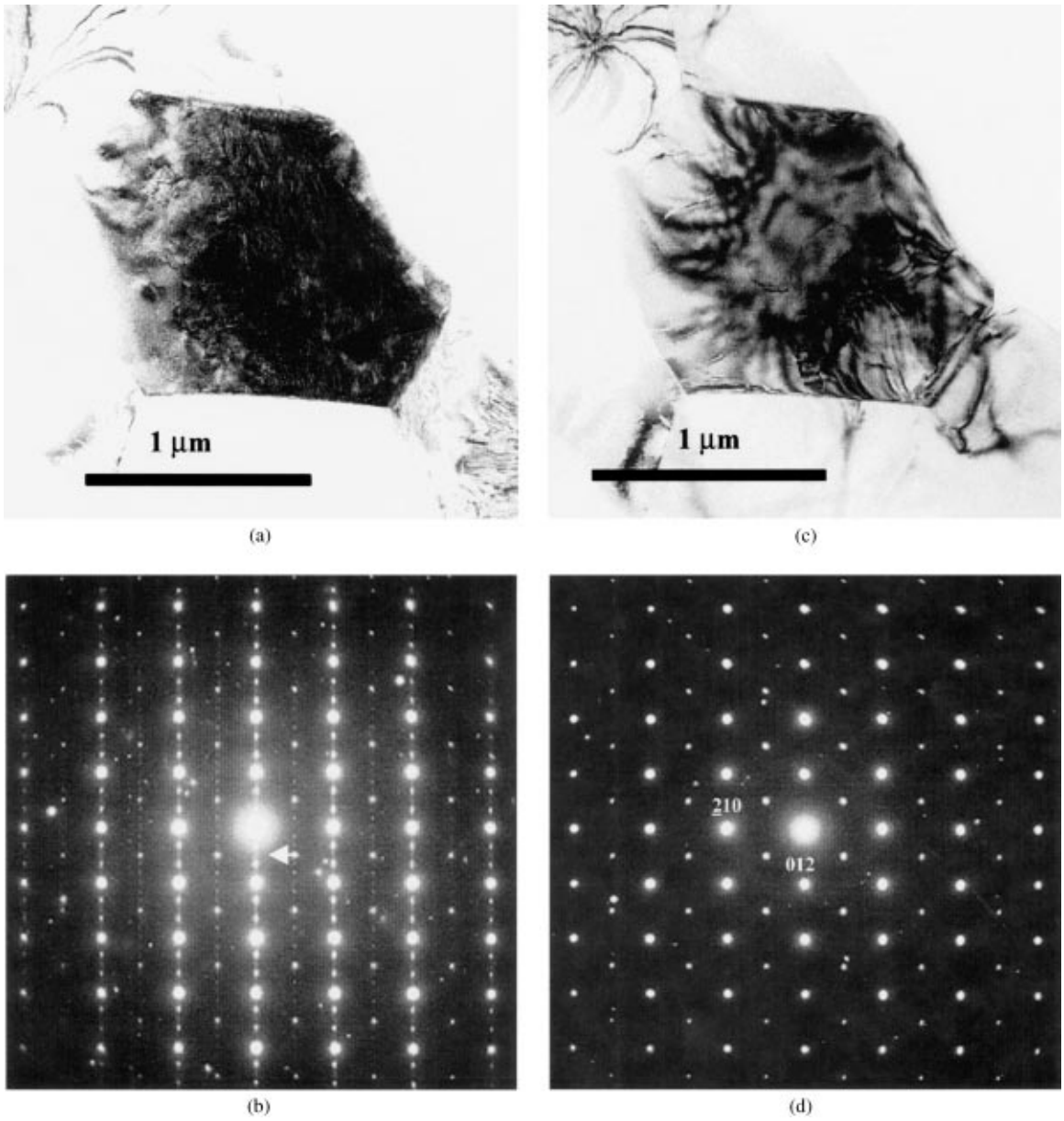

Figure 8 Material before (a, b) and after (c, d) beam heating experiment. (a) The bright-field image shows high density of defects before heating. (b) The corresponding SAD shows superstructure reflections (arrowed). (c) The bright-field image taken after beam heating shows that the high defect density has disappeared. No twin domains are present, but there is weak contrast from curved anti-phase like boundaries. (d) In the corresponding SAD pattern, superstructure reflections have disappeared.

upon cooling through the rhombohedral phase region (rhombohedral distortion and anisotropy increase with deceasing temperature).

Within weeks of sintering, long-scale residual strain is released when the material is thinned. This produced cracked TEM foils with significant macroscopic deformation. A high defect density is observed in the material and a deformation superlattice is observed. Once the deformation microstructure is formed, it is stable with respect to time at room temperature. Beam heating experiments showed that the metastable defect structure can be annealed and that this involves nanometre scale reordering of the structure but no reorientation of the basic crystal structure. Because the superstructures were observed in the non-substituted material, they cannot be attributed to ordering of different cations on the A sites. The commonly observed superstructure consisted in a tripling of the $\{100\}_c$ periodicity. A different superstructure, with a doubling of the $\{100\}_c$ periodicity, could also be observed. And in some diffraction patterns, a superposition of these situations could be observed. Close inspection of the diffraction patterns (e.g. Figs 5 and 7a) showed that the rotation of the axes due to the rhombohedral distortion of the lattice is reduced by the presence of the tripling (or doubling) superlattice. Care must be taken in making such measurements from highly faulted crystals because the intersection of the Ewald sphere with streaked reciprocal lattice points can change the position of reflections in the diffraction pattern. However, examination of several $\langle 100 \rangle_c$ diffraction patterns seems consistent with the conclusions drawn from examination of Figs 5 and 7.

Samples prepared 5 months or more after the pellets were fabricated did not generally show the behaviour described above. The thinned region of the sample remained flat, suggesting no residual strain remained in

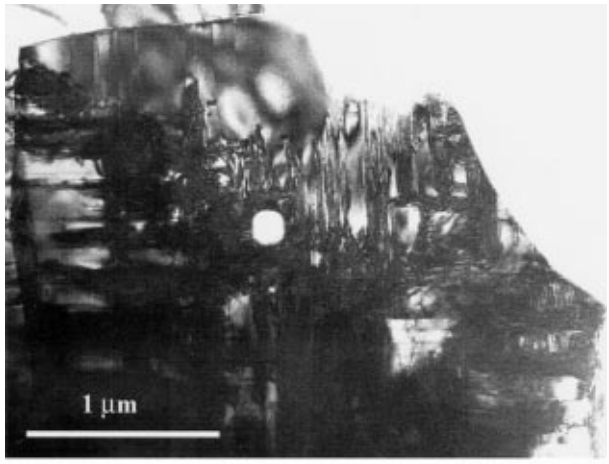

(a)

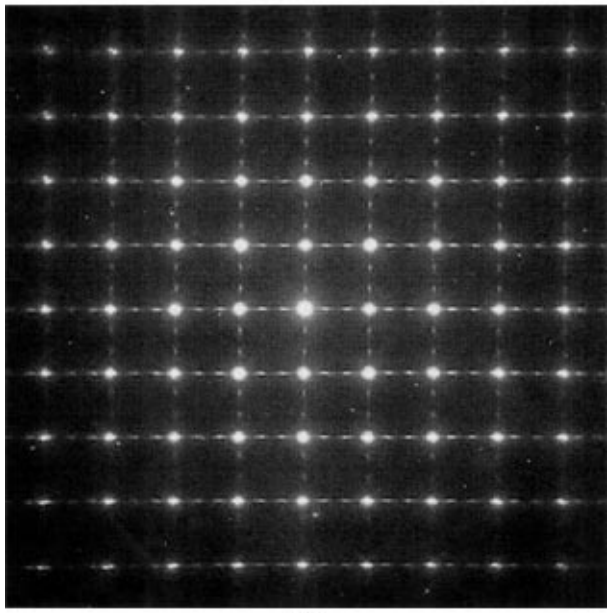

(b)

Figure 9 Grain in pre-cracked material prepared after >5 months. (a) Bright-field image showing defect-free regions within grain, as well as regions with high defect density (b) Corresponding SAD pattern from two superimposed sets of domains showing tripling superstructure along both $\langle 200 \rangle_c$ directions.

the material. No superlattice reflections were generally observed in diffraction patterns. For undeformed material, the main defects observed in the grains are $\{100\}_c$ twin domains. These twins reflect the reduction of symmetry during the cubic to rhombohedral phase transition during cooling, and provide a response in the material to spontaneous strain. Such strain can be produced by the change of shape of the unit cell in the phase transition [13]. It can also be produced by thermal stresses upon cooling through the rhombohedral phase region, owing to the anisotropic coefficient of thermal expansion of the rhombohedral phase. The geometry of the small number of stacking faults that we observed is consistent with the pseudo cube plane being the habit plane for defects in the rhombohedral perovskite structure. The density of perfect lattice dislocations is very low. Comparison of samples from symmetrically equivalent positions from either end of the original $LaCoO_3$ pellet, at different times, suggests that the variations observed in microstructure do not depend on variations in composition through the pellet.

The residual strain, high defect density and superlattice observations reported were unexpected. Wang and Zhang [7, 8] reported a superlattice in cubic $La_{0.5}Sr_{0.5}CoO_3$ which produced a doubling of the periodicity in the {200} planes. However, this was attributed to ordering of La and Sr cations in tetragonal domains with sizes of 30–200 nm. The superlattice observed here appears to be due to periodically spaced faults rather than being related to composition modulations. The most widely observed superlattice structure appears to be associated with periodic faults that combine to produce a defect structure that gives a tetragonal distortion of the rhombohedral structure of the material. The overall periodicity is three times that of the "ideal" perovskite cell and may be produced by repeating three distinct short displacement vectors in the faults. High resolution TEM imaging would be needed to provide more detail about the displacement vector associated with the faulting that produces the superlattice structures.

For some phase transformations, structural relaxation can be slow. Salje [13] discusses the example of the C/2*m*-C1 phase transition in Na-feldspar, where the Al, Si ordering component of the phase transition may not be observable on a laboratory time-scale below a temperature of 700 K. For the materials considered here, it seems important to consider the microscopic details of the cubic-to-rhombohedral phase transformation and the accommodation of the variation in rhombohedral angle below the transition temperature. A full discussion of these issues is beyond the scope of this paper. It is worth emphasizing, however, that the observed microstructures are very similar for all compositions, even though the structural transition occurs at different temperatures for the different compositions. Our observations furthermore suggest that the kinetics of thermal-strain accomodation proceed on a laboratory timescale, i.e. within months.

Up to the present time, no heating stage experiments have been performed. It would be useful to measure the temperature at which the defect structure was annealed from the specimens and observe the transformation in a more controlled manner than that achieved in the beam heating experiment described above. The high level of residual strain and associated deformation in thinned foils suggests that the bulk microstructure in the metastable transitional state is not accessible directly by the TEM. The thin foils are clearly modified by deformation during thinning. It would be desirable to use a non-destructive method for characterising the microstructure that is sensitive to defects present in the bulk material. The standard XRD measurements obtained from our materials were consistent with the expected single-phase rhombohedral perovskite structure. More detailed diffractometry, x-ray precession, or synchrotron XRD experiments may be sensitive to the presence of structural defects or domain structures in the rhombohedal matrix. The cooling rate for our samples was quite rapid on the scale over which subsequent changes appear to have taken place. Examination of similar material with differing post-sintering cooling rated might be considered.

It is interesting to relate our microstructural observations to recent observations of ferroelastic behaviour in Ca-substituted $LaCoO_3$, as witnessed by mechanical hysteresis and characteristic change in XRD patterns after surface machining [11]. The generally suggested micromechanism of ferroelastic behaviour is that of domain switching upon applied stress that exceeds the material's coercive stress [13]. The rhombohedral distortion can be regarded as a compressive strain along one of the $\langle 111 \rangle_c$ axes. There are four different variants of this distortion, one for each of the cubic $\langle 111 \rangle$ directions. The obvious domain-switching mechanism is between the different variants of rhombohedral distortion. Such a mechanism would involve a re-bending of Co-O-Co bonds and a rotation of octahedra and would result in a stretching of the originally compressed $\langle 111 \rangle$ direction and a compression of one of the previously stretched $\langle 11\underline{1} \rangle$ directions. The domains observed by TEM (e.g. Fig. 3) can be considered as orientation variants corresponding to compression along different $\langle 111 \rangle_c$ axes. It appears that the domain switching proposed as an underlying mechanism for the observed mechanical hysteresis [11], is not simply that of switching domains like the ones seen in Fig. 3 into the orientation of their neighbours. XRD after surface machining exhibits a significant line broadening, which doesn't disappear upon annealing, and which is indicative of a decrease in domain size. It is yet unclear whether or how the introduction of a fine domain structure upon mechanical loading is related to our observed heavily deformed microstructures.

Understanding the differences in behaviour and defect content of different TEM foils may also be relevant to industrial applications. Applications of these materials, as described in the introduction, for permeable membranes or as cathode materials, require stable physical and mechanical properties. For example, the development of cracks in a thin permeable membrane during use would be unacceptable. Particular attention should be given to applications where the materials are thermally cycled, either within the rhombohedral phase region or through the rhombohedral-to-cubic transition temperature. An understanding of the microstructural mechanisms of accomodation of spontaneous strain under such conditions will be important.

5. Conclusions

TEM observations from $LaCoO_3$, $La_{0.8}Sr_{0.2}CoO_3$, and $La_{0.8}Ca_{0.2}CoO_3$ revealed microstructures that were strongly influenced by the time of thin foil preparation. Thin foils prepared within the first weeks of sintering showed macroscopic strain and a very high defect density, which included fault-related superlattice structures. Samples prepared several months after sintering, showed no significant macroscopic strain and the main defect was found to be domain boundaries due to reflection twinning in the pseudo-cube plane. The observations revealed no obvious composition-related microstructural differences.

The pattern of behaviour is likely to be related to accomodation of spontaneous strain arising upon cooling of the material from the sintering temperature. The observations suggest that part of the local ordering associated with accomodation of strain takes place on a laboratory timescale of months. The presence of twin domains illustrate clearly the lowering of lattice symmetry as compared to the ideal cubic perovskite structure, and is relevant for explaining recent observations of ferroelastic behaviour of these materials.

Acknowledgement

The work described in this paper was funded by the Norwegian Research Council.

References

1. R. CACIUFFO, D. RINALDI, G. BARACCA, J. MIRA, J. RIVAS, M. A.SENARIS-RODRIGUEZ, P. G. RADAELLI, P. G. FIORANI and J. B. GOODENOUGH, *Phys. Rev. B* **59** (1999) 1068.
2. J. A. M. VAN ROOSMALEN and E. H. P. CORDFUNKE, *J. Sol. State Chem.* **93** (1991) 212.
3. J. MIZUSAKI, Y. MIMA, Y. SHIGERU, F. KAZUO and T. HIROAKI, *ibid.* **80** (1989) 102.
4. A. MINESHIGE, M. INABU, T. YAO, O. ZEMPACHI, K. KIKUCHI and K. MASAYA, *ibid.* **121** (1996) 423.
5. Y. TERAOKA, K. NOBUNAGA, N. MIURA and N. YAMAZOE, *Solid State Ionics* **48** (1991) 207.
6. H. TAGUCHI, M. SHIMADA and M. KIOZUMI, *J. Sol. State Chem.* **44** (1982) 254.
7. Z. L. WANG and J. ZHANG, *Phys.Rev. B* **54** (1996) 1153.
8. *Idem., Phil. Mag. A* **72** (1995) 1513.
9. B. GILBU, H. FJELLVÅG and A. KJEKSHUS, *Acta Chem. Scand.* **48** (1994) 37.
10. T. GRANDE *et al.* to be published.
11. K. KLEVELAND, A. M. MARDAL MOE, N. ORLOVSKAYA, T. GRANDE, M.-A EINARSRUD, K. BREDER and G. GOGOTSI, submitted to *Journal of American Ceramic Society*.
12. K. KLEVELAND, M.-A.EINARSRUD and T. GRANDE, *J. Eur. Ceram. Soc.* **20** (2000) 185.
13. E. H. K. SALJE, "Phase Transitions in Ferroelastic and Co-Elastic Crystals," (Cambridge Univ. Press, Cambridge, 1990).

Received 6 October 1999
and accepted 18 February 2000